Non-bonding Interaction of Dual Atom Catalysts for Enhanced Oxygen Reduction Reaction

Mohsen Tamtaji,[1] Qiuming Peng,[2] Tongchao Liu[3], Xue Zhao,[2] Zhihang Xu,[4] Patrick Ryan Galligan,[1] Md Delowar Hossain,[1] Zhenjing Liu,[1] Hoilun Wong,[1] Hongwei Liu,[1] Khalil Amine,[3] Ye Zhu,[4] William A. Goddard III,[5]* Wenting Wu,[6*] and Zhengtang Luo,[1]**

[1]Department of Chemical and Biological Engineering, Guangdong-Hong Kong-Macao Joint Laboratory for Intelligent Micro-Nano Optoelectronic Technology, William Mong Institute of Nano Science and Technology, and Hong Kong Branch of Chinese National Engineering Research Center for Tissue Restoration and Reconstruction, The Hong Kong University of Science and Technology, Clear Water Bay, Kowloon, Hong Kong, 999077, P.R. China

[2]State Key Laboratory of Metastable Materials Science and Technology, Yanshan University, Qinhuangdao 066004, P.R. China

[3]Chemical Sciences and Engineering Division Argonne National Laboratory 9700 Cass Ave, Lemont, IL 60439, USA

[4]Department of Applied Physics, Research Institute for Smart Energy, The Hong Kong Polytechnic University, Hong Kong, China

[5]Materials and Process Simulation Center (MSC), MC 139-74, California Institute of Technology, Pasadena CA, 91125, USA

[6]State Key Laboratory of Heavy Oil Processing, College of Chemistry and Chemical Engineering, Institute of New Energy, China University of Petroleum (East China), Qingdao 266580 (P. R. China)

Corresponding authors email: keztluo@ust.hk, wag@caltech.edu, wuwt@upc.edu.cn, and ye.ap.zhu@polyu.edu.hk

Abstract

We demonstrate the design of graphene-supported dual atom catalysts (DACs) for the four-electron oxygen reduction reaction (ORR), by utilizing the non-bonding interaction of counterpart metals (M) that synergistically tune the electronic properties and catalytic activity of the Fe site in $FeMN_6$-DAC and $FeMN_8$-DAC systems, where M stands for Fe, Co, Ni, Cu, and Zn. More specifically, for Fe-M distances below 15 Å, the non-bonding interaction is significant, making the system act as the DAC. We predicted that $FeNiN_6$-DAC and $FeNiN_8$-DAC exhibit a low ORR overpotential (η^{ORR}) of 0.28 V and 0.47 V, respectively, which are at the summits of volcano plots. This low ηO^{RR} originates from the high Bader charge transfer coupled with high spin density at the Fe site in both the $FeNiN_6$-DAC and $FeNiN_8$-DAC systems, which weakens the adsorption of OH* intermediate while enhancing desorption to H_2O. Guided by these density functional theory (DFT) computational results, we synthesized $FeCoN_8$-DAC and $FeNiN_8$-DAC along with N-doped graphene and confirmed their structures with scanning transmission electron microscopy (STEM), X-ray photoelectron spectroscopy (XPS), X-ray absorption near-edge structure (XANES), extended X-ray absorption fine structure (EXAFS), and electron spin resonance (ESR). We verify experimentally the catalytic activities and find that $FeNiN_8$-DAC has an experimental overpotential of 0.39 V with a Tafel slope of 47 $mVdec^{-1}$. Based on these results, we propose a DFT-guided strategy to tune the charge transfer and spin population of the active site toward designing DACs for electrochemical ORR.

Keywords: DFT, electrocatalyst, overpotential, spin state, descriptor

Introduction

Efficient oxygen reduction reaction (ORR) is essential for such applications as proton exchange membrane fuel cells (PEMFC) and Zin-air batteries to ensure rapid reaction kinetics [1]. Single atom catalysts (SACs) exhibit tunable electronic structures with high electrocatalytic ORR activity [2]. However, an unavoidable obstacle in the development of SACs is the scaling relationship limit. According to the scaling relationship limit there is normally a linear relationship between the adsorption energies of reaction intermediates (e.g., $\Delta G_{OOH*}=\alpha\Delta G_{OH*}+\beta$) which makes it impossible to tune independently the adsorption energy of a specific intermediate [3]. By introducing a second metal into SACs, leading to dual atom catalysts (DACs), the scaling relationship limit can be addressed by regulating the electronic structure and spin state of the metal centers towards high-performance electrochemical reactions [4]. Previous studies have devoted efforts on theoretical calculations and experimental synthesis to DACs for various electrochemical applications such as CO_2 reduction reaction (CO_2RR), hydrogen evolution reaction (HER), and ORR [5–11]. Although the bonding interaction through orbital coupling between the two metal centers is shown to be a tool useful for addressing the scaling relationship limit toward benefiting electrochemical reactions [12–17], the non-bonding interactions can also strongly affect their catalytic activity [18]. For example, regulating the spin state of Fe atoms has been accomplished by introducing Mn, leading to higher ORR activity [19]. In addition, non-bonding interaction of Ni counterpart metal on the CO_2RR activity of Fe atoms was previously reported to enhance CO_2RR [20]. That is, the presence of Ni metal can deliver charges through ligands to the Fe active metal to change its spin state and activity. It has been also experimentally shown that the combination of Fe and Ni atoms can surpass the ORR activity of each Fe and Ni SACs because of their long distance interaction [21]. It was then reported that the presence of counterpart Zn atom can affect the d-orbital electron distribution of Cu active site and facilitate the stretch and cleavage

of O-O. That is to facilitate the adsorption and desorption of reaction intermediates towards ORR [22]. However, the non-bonding interaction for electrocatalysis has not previously been investigated systematically. Therefore, the effect of counterpart metals on the spin population and charge transfer from active metal site to the reaction intermediates requires a fundamental study to tune the adsorption and desorption of reaction intermediates towards enhance electrochemical reactivity.

In this work, we use DFT calculations to examine the performance of $FeMN_6$-DAC and $FeMN_8$-DAC, where M stands for Fe, Co, Ni, Cu, and Zn as counterpart metals, towards ORR with $FeNiN_6$-DAC, and $FeNiN_8$-DAC at the summits of volcano plots. We found that the non-bonding interaction of these counterpart metals can significantly modify the ORR activity of Fe sites. Based on the feature importance analysis, we introduce a new intrinsic descriptor for the rational design of DACs towards ORR.

Inspired by these theoretical calculations, $FeCoN_8$-DAC and $FeNiN_8$-DAC along with N-doped sample were synthesized using a two-step pyrolysis approach. Accordingly, the local atomic structure of the DACs and their local surroundings was confirmed using X-ray photoelectron spectroscopy (XPS), X-ray absorption near-edge structure (XANES), extended X-ray absorption fine structure (EXAFS), scanning transmission electron microscope (STEM), and electron energy loss spectroscopy (EELS). The ORR activity of the synthesized DACs was measured, where we find a lower overpotential and higher activity for $FeNiN_8$-DAC, in agreement with our theoretical predictions. These results demonstrate that DFT-guided design of DACs can enable accelerated discovery of improved electrochemical activities, providing a new tool for their rational design.

Experimental section

Chemicals

An ethanol solution of 96% is obtained from the Merck Inc. of Germany. $KMnO_4$, H_2SO_4 (95%), acrylamide (AM, 99%), $FeCl_3$•$6H_2O$ (97%), $CoCl_2$•$6H_2O$ (99%), and $NiCl_2$•$6H_2O$ (98%) are all obtained from Sigma Inc. USA. Graphite (grafguard) is used with an average particle size of 350 mm. Ultrapure (18.2 MΩ) deionized water (DI) is used for washing purposes during the whole synthesis process. All chemicals mentioned above are used as received and utilized with no further treatments.

Synthesis of graphene oxide (GO)

GO is synthesized using the modified hummers method through the exfoliation and oxidation of expanded graphite sheets during thermal treatment [23]. Briefly, microwave-expanded graphite (1 g) is dispersed into 30 ml of H_2SO_4 (98%) inside a 500 ml round bottom flask, followed by stirring in an ice bath. After a duration of 2 hours, 5 g of $KMnO_4$ is slowly added to the suspension. Subsequently, the suspension is kept stirring at room temperature for 4 hours until the color became pale brownish. Then, the solution is slowly diluted with 50 ml of deionized (DI) water while the color change towards brown. After that, the solution is diluted with 200 ml of DI water while stirring for another 2 hours at room temperature. Finally, enough amount of H_2O_2 (30 wt.%) is added dropwise to the solution mixture to reduce the residual $KMnO_4$ until the solution's color is converted into bright green. The solution is stirred for another 2 hours and then allowed to settle for 1 day. The synthesized GO is then centrifuged and washed at least 9 times with DI water at 15000 rpm for 30 min. The centrifuged GO solution is ultimately reached to 8 mg/ml concentration by dispersing into DI water for further experiments.

Synthesis of DACs

Different types of catalysts supported by graphene are synthesized, namely, $FeCoN_8$-DAC and $FeNiN_8$-DAC, along with nitrogen-doped graphene (N-doped). Metal precursors, $FeCl_3$•$6H_2O$, $CoCl_2$•$6H_2O$, and $NiCl_2$•$6H_2O$ salts is dissolved to make 0.05 M solution of Fe^{3+}, Co^{2+}, and Ni^{2+}

respectively [24,25]. GO suspension is diluted by mixing 12.5 ml of 8 mg/ml GO into 120 ml DI water. 125 µl of 0.05 M of Fe^{3+} and Co^{2+} solutions and 1.2 ml of acrylamides (25 wt.%, as a nitrogen precursor) are added into the diluted GO suspension and stirred for 23 hours. The mixed solution is freeze-dried for four days and went through a two-step annealing process, as following, to synthesize highly dispersed DACs [26]. The brownish freeze-dried sample went through the first annealing step in a 1-inch quartz tube furnace at 300 ℃ for 3 hours under Ar (202 sccm). Then the blackish sample is washed using H_2SO_4 (0.05 M) and ethanol (96%) five times before being freeze-dried. Subsequently, the freeze-dried sample went through a second annealing process at 500 ℃ for 3 hours under Ar (202 sccm) to produce $FeCoN_8$-DACs. Similarly, $FeNiN_8$-DAC is prepared using 125 µl of 0.05 M of each Fe^{3+} and Ni^{2+} solution as the metal precursors in the procedure mentioned above. The control sample (N-doped) is prepared without adding a metal precursor.

Characterization and analysis

The structure and morphology of synthesized DACs were examined by transmission electron microscopy (TEM, JEOL JEM 100CXII) and scanning transmission electron microscopy (STEM, JEOL JEM-2100F) combined with electron energy loss spectroscopy (EELS) and scanning electron microscopy (SEM, JEOL JSM-7800F). Chemical structure verification, elemental composition, and elemental bonding states were extracted from X-ray photoelectron spectroscopy (XPS) with a PHI 5600 (Physical Electronics). All XPS spectra were corrected concerning the C 1s peak (284.48 eV). Energy dispersive x-ray analysis (EDX, JEOL JEM 100CXII, and JEOL JSM-7800F) was used for the elemental mapping. The Fe-K, Co-K, and Ni-K edge was acquired through the synchrotron radiation-based XAFS facility at Argonne Photon Source (APS) through the X-ray Absorption Spectroscopy (XAS) to investigate the local environment around metal atoms. ATHENA, ARTEMIS, and IFEFFIT analysis tools provided in the Demeter processing

package are used to analyze the obtained XAS and EXAFS data. DACs were then analyzed using XRD (PANalytical) and Raman (Renishaw Raman RM3000 scopes with a 514 nm laser source).

Electrocatalytic activity

The ORR test was conducted via taking 5 mg of each of N-doped, $FeCoN_8$-DAC, or $FeNiN_8$-DAC samples, 100 µL Nafion (5 wt.% in a mixture of lower aliphatic alcohols and water), 700 µl of DI water and 300 ml of ethyl alcohol. The mixture was sonicated for 10 min to get a homogeneous catalyst ink. Then, 30 µL of ink as a catalyst was loaded on a 5 mm diameter surface of the neat and clean, glassy carbon electrode (GCE). We used 5 mm diameter GCE for ORR performance, and three electrode cell was used for measurements and loaded with 0.5 M H_2SO_4 aqueous electrolyte for testing ORR. The loading for as-prepared catalyst is 0.375 mg cm^{-2}. The Ag/AgCl was used as a reference electrode which was prior filled in saturated KCl, while glassy carbon was used as a working electrode and Pt wire as a counter electrode. RHE potential was used via $E_{RHE}=E_{Ag/AgCl} + 0.197 + 0.0592\times pH$. Highly pure Ar (99.99%) and O_2 (99.99%) were purged to H_2SO_4 electrolyte for 30 min before testing our catalysts and measured the CV with a scan rate of 50 mVs^{-1}.

From positive to negative, the rotating speed (400, 800, 1200, 1600, and 2000 rpm) was used to measure the LSV polarization curve with the rate of seeping at 10 mV/s. Tafel slopes for ORR was obtained from corresponding LSV curves. The ORR Tafel slope for all catalysts is drawn against logarithmic scale current density versus working potential; all catalysts' ORR Tafel slope was determined. The ORR polarization curves of the $FeNiN_8$-DACs were also carried out at different rotation speed (400 rpm-2000rpm) to obtain Koutecky-Levich (K-L) plot based on the following equation [25]:

$$\frac{1}{j} = \frac{1}{B\omega^{1/2}} + \frac{1}{j_K} \quad (1)$$

$$B = 0.2nFC_0(D_0)^{2/3}v^{-1/6} \quad \text{and} \quad j_K = nFkC_0 \quad (2)$$

Where j is the measured current density, ω is the electrode rotation rate, F is the Faraday constant, C_0 is the bulk concentration of O_2, D_0 is the diffusion coefficient of O_2, v is the kinetic viscosity of the electrolyte.

DFT calculations

The atomic and electronic structures of DACs were computed using first-principles density functional theory (DFT) in Gaussian 09 software. Theoretical calculations were performed at the Becke, 3-parameter, Lee–Yang–Parr (B3LYP) exchange functional level of DFT along with 6-31G (d, p) basis set for the geometry optimizations. Also, the DFT-D3 method was used to include van der Waals interactions. We used the solvation model density (SMD) as a universal continuum solvation model to include solvent effects (H_2O) [27]. The effect of magnetic coupling was considered in all the DFT calculations [13]. Electron density and projected density-of-states (DOS) were generated with the Multiwfn 3.8 program [28]. We calculated the vibrational frequencies to obtain Gibbs free energies for analyzing the ORR reaction mechanism. According to previous studies the Fe atom is the active site for ORR, so only the Fe based sites were considered for this study [29].

Results and discussion

First, we calculated the Gibbs free energy profiles of $FeMN_8$-DAC and $FeMN_6$-DAC (M: Fe, Co, Ni, Cu, and Zn) for ORR. **Scheme1a** shows the structure of $FeMN_6$-DAC and $FeMN_8$-DAC with Fe-M distances of 7.58 Å and 2.58 Å, respectively. The distances are measured based on the optimized structure without any adsorbate. The green semi circles indicate the non-bonding effect of M counterpart metals which can deliver charges through the intervening ligands to the Fe active

metal to modify its spin state and ORR activity. **Scheme1b** indicates the lateral view of ORR intermediates, indicating the spin-crossover of Fe site during ORR [30]. In fact, the interaction between the π* orbital of the reaction intermediates and the d orbitals of Fe site leads to changes in both the d-orbital splitting and the delocalization of electrons from low-lying d_{xy} and d_{yz} orbitals to the high-lying d_{x2-y2} orbital of Fe [30]. As shown in **Scheme 1b**, the ORR may proceed through the following fundamental steps, which are normally used to investigate electrocatalysis of the ORR on the Fe active site [31]:

$$* + H_2O \rightleftharpoons OH^* + H^+ + e^- \quad (3)$$

$$* + H_2O \rightleftharpoons O^* + 2H^+ + 2e^- \quad (4)$$

$$* + 2H_2O \rightleftharpoons OOH^* + 3H^+ + 3e^- \quad (5)$$

$$* + 2H_2O \rightleftharpoons O_2^* + 4H^+ + 4e^- \quad (6)$$

Because it is difficult to obtain the exact free energy of OOH, O, OH, and H radicals in the electrolyte solution, the Gibbs free energies of ΔG_{OOH*}, ΔG_{O*}, ΔG_{OH*}, and ΔG_{H*} are relative to the free energy of stoichiometrically appropriate amounts of H_2O (g) and H_2 (g), defined as follows [31]:

$$\Delta G_{OH*} = E_{DAC-OH^*} - E_{DAC} + \frac{1}{2}E_{H_2} - E_{H_2O} + \Delta ZPE - T\Delta S \quad (7)$$

$$\Delta G_{O^*} = E_{DAC-O^*} - E_{DAC} + E_{H_2} - E_{H_2O} + \Delta ZPE - T\Delta S \quad (8)$$

$$\Delta G_{OOH*} = E_{DAC-OOH^*} - E_{DAC} + \frac{3}{2}E_{H_2} - 2E_{H_2O} + \Delta ZPE - T\Delta S \quad (9)$$

$$\Delta G_{O_2^*} = E_{DAC-O_2^*} - E_{DAC} + 2E_{H_2} - 2E_{H_2O} + \Delta ZPE - T\Delta S \quad (10)$$

E_{H2} and E_{H2O} represent the energy of gas phase H_2 and H_2O, respectively. $E_{DACs-H*}$, $E_{DACs-OH*}$, $E_{DACs-O*}$, and $E_{DACs-OOH*}$ are the total energy of DACs with adsorbed H, OH, O, and OOH states,

respectively. E_{DACs} is the energy of DAC surface, ΔZPE is zero-point energy (ZPE) correction, TΔS is entropy correction, and T is the temperature.

The adsorption free energies of ORR are approximately independent of the pH of the solution [29]. The difference between the equilibrium potential of U=1.23 V and the limiting potential is the theoretical ORR overpotential (η^{ORR}), and limiting potential is the highest potential at which all the reaction steps are downhill in free energy (see section S2 of Supporting Information) [32]. The reaction step which is flat in free energy at the limiting potential is the rate determining step [32]. **Figure 1a** illustrates the Gibbs free energies diagram of reaction intermediates for $FeNiN_6$-DAC (see **Figure S10-S12** for other $FeMN_6$-DAC and $FeMN_8$-DAC). **Figure 1a** shows that the formation of H_2O from OH* is the ORR rate-determining step, because this reaction step, which is shown as a blue dashed circle, is flat in free energy at the limiting potential of 0.95. From **Figure 1a**, we find that the ORR limiting potential and η^{ORR} of $FeNiN_6$-DAC are 0.95 V and |1.23-0.95|=0.28 V, respectively. **Figure 1b** shows the volcano plot of theoretical η^{ORR}, obtained from **Figure S10-S12**, versus the number of d electrons of the counterpart metal (M). We found that $FeNiN_6$-DAC and $FeNiN_8$-DAC are both at the summit with the η^{ORR} of 0.28 V and 0.47 V, respectively, which are comparable with theoretically obtained η^{ORR} of 0.43 V for the benchmark Pt(111) [31], 0.33 V for $CoRu@N_8V_4$ [33], and 0.34 for $CoCuN_6$-gra(OH) [13]. In contrast, the $FeCuN_8$-DAC and $FeZnN_8$-DAC possess unfavorable theoretical η^{ORR} of 0.68 V and 0.83 V, respectively. **Figure S16** displayes the counter plot of η^{ORR} versus the d electrons of M and Fe-M distance (D_{Fe-M}), suggesting that the ORR overpotential increases with the Fe-M distance. Our evaluation on the DAC systems revealed that for D_{Fe-M}<15 Å, the system acts as a DAC, while for D_{Fe-M}>15 Å, the M atom has no significant impact on the catalytic activity of active site, so the system acts as a SAC.

To shed more light on the effect of counterpart M metals on the ORR activity of Fe site, we plotted the projected density of states (PDOS) for the Fe sites. **Figure 1c** shows the PDOS of 3d orbitals at the Fe site in $FeNiN_6$-DAC before and after interaction with OH*. Some peaks disappeared and other peaks evolved after interacting with OH*. The new peaks are designated as bonding (σ) and antibonding (σ*) orbitals, indicating the interaction of the Fe site with OH* [24]. **Figure S13** shows the PDOS of 3d orbitals of Fe site for $FeNiN_6$-DAC and FeN_4-SAC systems, indicating that the active valence $3d_{z2}$ orbital of the Fe in $FeNiN_6$-DAC shifted down, weakening the interaction with reaction intermediates. Thus, the reaction activity of Fe site in $FeMN_6$-DAC and $FeMN_8$-DAC structures strongly depends on the non-bonding interaction between Fe and the counterpart metals (M).

According to **Figure 1b** and **Figure S16**, our results show that the ORR catalytic activity of Fe metal depends strongly on the number of d electrons of counterpart metal (M). This agrees with the feature importance analysis performed using the machine learning (ML) [34,35] technique on the Gibbs free energy of ORR intermediates, which suggested that the electronegativity and d electron numbers of the counterpart M metal as the most important parameters (**Figure S32**). Insired by the feature importance analysis shown in **Figure S32**, a simple descriptor (φ) is introduced to consider the effect of most important parameters describing the ORR activity of DACs:

$$\varphi = \frac{\left|\theta_{d,M} - 1.33\theta_{d,Fe}\right|}{E_M} - \frac{D_0}{D_{Fe-M}} \tag{11}$$

θ_d is the number of d orbital valence electrons of M, E_M is the electronegativity of M, D_0 is the closest distance btween Fe and M metals (2.58 Å), and $D_{Fe\text{-}M}$ is the distance between Fe and M metals (between D_0=2.58 Å and 15 Å). As shown in **Figure 1d**, η^{ORR} increases linearly with the

descriptor φ. Similarly, as shown in **Figure S28**, the new descriptor satisfactory defines the η^{ORR}, Gibbs free energy of reaction intermediates and spin population of Fe site.

As shown in **Table S2**, the Mulliken charge of Fe is 1.238, 1.332, 1.321, 1.253, 1.193, 1.264, 1.311, 1.302, 1.269, and 1.283 e^-, respectively, for $FeFeN_8$-DAC, $FeCoN_8$-DAC, $FeNiN_8$-DAC, $FeCuN_8$-DAC, $FeZnN_8$-DAC, $FeFeN_6$-DAC, $FeCoN_6$-DAC, $FeNiN_6$-DAC, $FeCuN_6$-DAC, and $FeZnN_6$-DAC. As shown in **Figure S17**, a specific charge is transfered from Fe atom to the conterpart metals (M) which depends directly on the electronegativity of the counterpart M atom. Thus, a relatively high charge is transferred from Fe to Ni site (**Figure S18**) [36], increasing the oxidation state of Fe site, weakening the adsorption of *OH intermediate [37,38], and decreasing the ORR overpotential [39] by increasing the spin density of Fe site (**Figure 2a**). These results are in great agreement with the electron spin resonance (ESR) specroscopy results for N-doped, $FeCoN_8$-DAC, and $FeNiN_8$-DAC at 77 K, which are shown in **Figue 2b**. The g values of around 2.00 in the ESR spectra are assigned to the unpaired electron in the $3d_{z2}$ and $3d_{x2-y2}$ orbitals of Fe^{2+} [40]. The ESR spectrum for $FeNiN_8$-DAC indicates a stronger signal than $FeCoN_8$-DAC, while this signal disappears in N-doped graphene, suggesting additional unpaired 3d electrons for Fe in the $FeNiN_8$-DAC system [19,41,42]. In addition, **Figure 2c** shows high charge transfer between $FeNiN_6$-DAC and the OH* intermediate, in agreement with recent work [43]. **Figures 2d-e** indicates high spin polulation of Fe site in $FeNiN_6$-DAC and yet its high charge transfer, facilitates OH* desorption to release H_2O, which makes this configuration a promising catalyst for ORR [22,44].

Based on the above calculations, we synthesized $FeCoN_8$-DAC and $FeNiN_8$-DAC along with N-doped graphene samples. The chemical states and compositions of the prepared samples were studied with X-ray photoelectron spectroscopy (XPS). The XPS results show the Fe and Co metal contents to be 0.20 and 0.18 wt.% respectively, in the $FeCoN_8$-DAC sample. The Fe and Ni metal

contents are 0.19 and 0.18 wt.% respectively, in the $FeNiN_8$-DAC sample. This suggests an Fe/Ni and Fe/Co molar ratios of around 1:1. To identify different types of nitrogen in the DACs, we deconvoluted the N 1s peak, suggesting different types of nitrogen for $FeNiN_8$-DAC, and N-doped samples. For example, **Figure S1b** shows that the N 1s peak for $FeNiN_8$-DAC deconvoluted into pyridinic-N (398.1 eV), Fe-N (398.7 eV), pyrrolic-N (400.1 eV), and oxidized-N (406.9 eV) [24]. **Figure 3a-c** shows a high-resolution peak spectrum for Fe, Co, and Ni metals of the synthesized samples, indicating two valence states ($p_{1/2}$ and $p_{3/2}$) for Fe, Co, and Ni with the partially oxidative states [20,29]. The binding energy of Fe $2p_{3/2}$ in $FeNiN_8$-DAC shifts by +0.1 eV compared with that in $FeCoN_8$-DAC, suggesting a lower valence state for Fe [20]. This is in agreement with the Mulliken charge analysis of Fe, changing from 1.332 e^- to 1.104 e^-, respectively, for $FeCoN_8$-DAC and $FeNiN_8$-DAC, suggesting that the Ni atom donates fewer electrons to Fe atom than does Co [45].

The electronic states and atomic configuration of the metal atoms in the synthesized samples were further investigated with the XANES and EXAFS. **Figure 3d-f** show the metal K-edge XANES spectra for $FeCoN_8$-DAC and $FeNiN_8$-DAC, indicating that the local atomic structure around Fe, Co, and Ni metal atoms is distinct from their bulk metals. **Figure 3d-f** indicates a blue-shift in the absorption edge of these metals compared to their bulk sample, suggesting a valence state higher than 0. We attribute the higher valence state to coordination between the metals and the N8 coordination [24,25,40]. Moreover, three peaks for Fe atom in **Figure 3d** indicate to 1s→3d, 1s→$4p_z$, and 1s→$4p_{xy}$ transitions [40]. The differences in intensity of peak C as the main edge peak in **Figure 3d1** is confirmed by the existence of divacancy-based M-N_4C_4 moieties bonded axially with broken D4h symmetry [24]. In addition, we observe a downshift in the main peak C of the K-edge XANES spectra of $FeNiN_8$-DAC compared to $FeCoN_8$-DAC, suggesting

delocalization of unpaired electrons in the high-lying d_{z2} orbital of Fe onto ligands [30], more clearly shown through the spin density in **Figure S14**. In addition, as shown in the inset of **Figure 3a**, the Fe K-edge XANES spectra of $FeCoN_8$-DAC shows a red-shift in the adsorption edge compared to $FeNiN_8$-DAC, indicating a decreased valence of Fe in $FeCoN_8$-DAC [45], in agreement with the XPS results. The red-shift in the Fe K-edge XANES spectra can be obtained from theory using the accurate finite difference (FD) approach implemented in the FDMNES software [24,46], shown in **Figure S33**.

In addition, the bonding and coordination environment around the metal in the DACs were further studied using EXAFS Fourier transform (FT) for $FeCoN_8$-DAC and $FeNiN_8$-DAC. **Figure 3g-i** shows that the EXAFS FT spectra of $FeCoN_8$-DAC and $FeNiN_8$-DAC exhibit primary peaks corresponding to Fe-N bonding at around 1.42 Å, different from the Fe-O peak at 1.55 Å [29] and Fe-Fe peaks at 2.17 and 4.48 Å. The EXAFS FT spectra for the $FeCoN_8$-DAC sample exhibits a primary peak attributed to Co-N at 1.40 Å, different from the Co-O peak at 1.63 Å [47] and Co-Co peaks at 2.15 and 4.20 Å. Similarly, the EXAFS FT spectra for the $FeNiN_8$-DAC sample exhibits a primary peak attributed to Ni-N bonding at 1.43 Å, different from the Ni-O peak at 1.62 Å [47] and Ni-Ni peaks at 2.17 and 4.19 Å. These results confirm that the coordination environment around the metal atoms corresponding to metal-N interaction.

Figure 4a and **4c** shows the STEM images of $FeCoN_8$-DAC and $FeNiN_8$-DAC samples, respectively, where the individual metal atoms (white dots) distribute homogeneously throughout the whole graphene support. EELS analysis on the specimen confirms that the brighter dots are Co/Fe atoms in the $FeCoN_8$-DAC sample and Fe/Ni atoms in the $FeNiN_8$-DAC sample, as shown in Figure 4b and 4d, respectively. The surface structure, morphology, and elemental mapping of $FeCoN_8$-DAC and $FeNiN_8$-DAC are confirmed by SEM images (**Figure S2**). **Figures S3** and **S4**

show the SEM imaging and EDX elemental mapping for Fe, C, N, Co, and Ni elements, confirming the uniform presence of all elements. **Figure S5b** also shows the TEM image for the $FeNiN_8$-DAC sample, suggesting the uniform dispersion of the Fe and Ni metal atoms without noticeable aggregation. The results are consistent with an XRD spectrum provided in **Figure S6** for N-doped, $FeCoN_8$-DAC, and $FeNiN_8$-DAC samples. The XRD spectra features only one broad graphitic carbon peak (002) at 23.3º. No other peak is detected that would correspond to metal species or their compounds with oxides or nitrides [24]. **Figure S5a** displays the STEM image for the $FeNiN_8$-DAC sample, suggesting the rich porous support, which is in consistent with a Raman spectrum provided in **Figure S7**. As shown in **Figure S7**, the intensity ratio of D/G-band (I_D/I_G) in the Raman spectra increases from 0.701 to 0.902 and the density of defect vacancies (n_D) increases from 2.12 nm^{-2} to 2.73 nm^{-2} for graphene oxide (GO) and $FeNiN_8$-DAC sample, respectively, correlating to the expected rise in defect density due to N doping, the addition of metallic species and greater disruption of the hexagonal lattice (see Supporting Information for more details) [48].

The ORR performance of all synthesized materials was checked, including rotating disk electrode tests in acidic medium, 0.5 M H_2SO_4. As shown in **Figure 5a**, the reduction current appears at +0.84 V versus RHE for the $FeNiN_8$-DAC sample, corresponding to a very low overpotential of 1.23-0.84 = 0.39 V, which is comparable to our theory obtained overpotential of 0.47 V, **Figure 1b**. However, for $FeCoN_8$-DAC and N-doped the onset potential was more negative than $FeNiN_8$-DAC. The as-synthesized DACs are judged through Tafel slope values resulting from corresponding ORR curves shown in **Figure S9**. Out of all samples, the $FeNiN_8$-DAC sample delivered the lowest Tafel slope of 47 $mVdec^{-1}$, comparable with 60 $mVdec^{-1}$ obtained for Fe/Ni-Nx/OC [49]. This value is significantly lower than the Tafel slope values of $FeCoN_8$-DAC (65

mVdec^{-1}) and N-doped graphene (64 mVdec^{-1}), suggesting that the $FeNiN_8$-DAC has favorable reaction kinetics for ORR applications. This agrees with our DFT results in **Figure 1b**, showing that $FeNiN_8$-DAC has a lower overpotential than $FeCoN_8$-DAC. Cyclic voltammetry (CV) measurements of $FeNiN_8$-DAC were carried out in 0.5 M H_2SO_4 acidic solution at a scan rate of 50 mVs^{-1} under saturated O_2 and Ar, as shown in **Figure 5b**. The CV curve of $FeNiN_8$-DAC under O_2 revealed a prominent ORR peak (red line) at 0.72 V versus RHE, while the corresponding peak is absent under Ar-saturated electrolyte (black line). This shows that O_2 is reduced by $FeNiN_8$-DAC. **Figure 5c** displays the ORR polarization curves of the $FeNiN_8$-DAC with various rotation speeds of 400 to 2000 rpm, indicating higher reaction rates for higher rotation speeds. The K-L plots for the applied potentials of 0.30, 0.35, and 0.40 V are shown in **Figure 5d**, indicating good linearity for all applied potentials. B =0.15 in equation 2 is determined from the slope of the K-L equation and the ORR kinetic current density, j_K = 22.5 mAcm^{-2} , is calculated from the K-L plot, which is comparable to j_K = 28.1 mAcm^{-2} obtained for Fe/Ni-Nx/OC [49], suggesting a proficient electron transfer process. Besides, a cycling stability test was carried out to investigate the long-lasting durability of the $FeNiN_8$-DAC in O_2-saturated electrolytes. As shown in **Figure S8**, after 550 cycles at the scan rate of 2000 mVs^{-1} and the potential window between 0 and 1.5 V (versus RHE), the $FeNiN_8$-DAC possesses its original onset potential, while the current density decreased a little, indicating its satisfactory stability.

Conclusion

We demonstrate the design of graphene-supported dual atom catalysts (DACs) for four-electron oxygen reduction reaction (ORR) using density functional theory (DFT) calculations validated with experiments. We observed that the non-bonding interaction of counterpart metals (M: Fe, Co, Ni, Cu, and Zn) plays an important role in lowering the ORR overpotential of Fe sites in $FeMN_6$-

DAC and $FeMN_8$-DAC structures. More specifically, $FeNiN_6$-DAC and $FeNiN_8$-DAC exhibit low ORR overpotentials of 0.28 V and 0.47 V, respectively, as compared with 0.71 V for FeN_4-SAC. In addition, based on the feature importance analysis, we introduce a new intrinsic descriptor to describe the properties of these DACs towards ORR. Guided by these computational results, we synthesized $FeCoN_8$-DAC and $FeNiN_8$-DAC along with N-doped graphene and confirmed their structures with scanning transmission electron microscopy (STEM), X-ray photoelectron spectroscopy (XPS), X-ray absorption near-edge structure (XANES), and extended X-ray absorption fine structure (EXAFS). Subsequently, we measured the catalytic activity of $FeCoN_8$-DAC and $FeNiN_8$-DAC for ORR. We found that $FeNiN_8$-DAC demonstrates a higher catalytic activity with overpotential of 0.47 V, comparable to 0.43 V for the benchmark Pt/C. Based on these results, we propose a DFT-guided strategy for designing $FeMN_6$-DAC and $FeMN_8$-DAC for electrochemical ORR.

Acknowledgements

Z.L. acknowledge supports by RGC (16304421), and the IER foundation (HT-JD-CXY-201907), "International science and technology cooperation projects" of Science and Technological Bureau of Guangzhou Huangpu District (2019GH06), Guangdong Science and Technology Department (Project#:2020A0505090003), Research Fund of Guangdong-Hong Kong-Macao Joint Laboratory for Intelligent Micro-Nano Optoelectronic Technology (No. 2020B1212030010). Technical assistance from the Materials Characterization and Preparation Facilities of HKUST is greatly appreciated. Q.P. thanks the Natural Science Foundation of Hebei Province for Innovation Groups Program (C2022203003). Y.Z. thanks the financial support from the Hong Kong Polytechnic University (Grant No. ZVRP). WAG thanks the US National Science Foundation (CBET-2005250) for support.

Associated Content

Supporting Information

Characterization, DFT calculations, Descriptor, and Machine Learning (ML) on Gibbs free energy.

Conflicts of interest

These authors respectfully declare that there are no conflicts of interest to acknowledge for this research.

References

[1] X. Li, Z. Xiang, Identifying the impact of the covalent-bonded carbon matrix to FeN4 sites for acidic oxygen reduction, Nat. Commun. 13 (2022). https://doi.org/10.1038/s41467-021-27735-1.

[2] Y. Wu, Q. Wu, Q. Zhang, Z. Lou, K. Liu, Y. Ma, Z. Wang, Z. Zheng, H. Cheng, Y. Liu, Y. Dai, B. Huang, P. Wang, An organometal halide perovskite supported Pt single-atom photocatalyst for H 2 evolution , Energy Environ. Sci. 15 (2022) 1271–1281. https://doi.org/10.1039/d1ee03679c.

[3] L. Li, K. Yuan, Y. Chen, Breaking the Scaling Relationship Limit: From Single-Atom to Dual-Atom Catalysts, Accounts Mater. Res. (2021). https://doi.org/10.1021/accountsmr.1c00264.

[4] F. Rehman, S. Kwon, C.B. Musgrave, M. Tamtaji, W.A. Goddard, Z. Luo, High-throughput screening to predict highly active dual-atom catalysts for electrocatalytic reduction of nitrate to ammonia, Nano Energy. 103 (2022) 107866. https://doi.org/10.1016/j.nanoen.2022.107866.

[5] J. Wang, Z. Huang, W. Liu, C. Chang, H. Tang, Z. Li, W. Chen, C. Jia, T. Yao, S. Wei, Y. Wu, Y. Li, Design of N-Coordinated Dual-Metal Sites: A Stable and Active Pt-Free Catalyst for Acidic Oxygen Reduction Reaction, J. Am. Chem. Soc. 139 (2017) 17281–17284. https://doi.org/10.1021/jacs.7b10385.

[6] M. Feng, X. Wu, H. Cheng, Z. Fan, X. Li, F. Cui, S. Fan, Y. Dai, G. Lei, G. He, Well-defined Fe-Cu diatomic sites for efficient catalysis of CO2electroreduction, J. Mater. Chem. A. 9 (2021) 23817–23827. https://doi.org/10.1039/d1ta02833b.

[7] Z. Zeng, L.Y. Gan, H. Bin Yang, X. Su, J. Gao, W. Liu, H. Matsumoto, J. Gong, J. Zhang, W. Cai, Z. Zhang, Y. Yan, B. Liu, P. Chen, Orbital coupling of hetero-diatomic nickel-iron site for bifunctional electrocatalysis of CO2 reduction and oxygen evolution, Nat. Commun. 12 (2021) 1–11. https://doi.org/10.1038/s41467-021-24052-5.

[8] N. Karmodak, S. Vijay, G. Kastlunger, K. Chan, Computational Screening of Single and Di-Atom Catalysts for Electrochemical CO 2 Reduction , ACS Catal. (2022) 4818–4824.

https://doi.org/10.1021/acscatal.1c05750.

[9] Y. Cheng, S. He, J.P. Veder, R. De Marco, S. ze Yang, S. Ping Jiang, Atomically Dispersed Bimetallic FeNi Catalysts as Highly Efficient Bifunctional Catalysts for Reversible Oxygen Evolution and Oxygen Reduction Reactions, ChemElectroChem. 6 (2019) 3478–3487. https://doi.org/10.1002/celc.201900483.

[10] Z. Xiao, P. Sun, Z. Qiao, K. Qiao, H. Xu, S. Wang, D. Cao, Atomically dispersed Fe-Cu dual-site catalysts synergistically boosting oxygen reduction for hydrogen fuel cells, Chem. Eng. J. 446 (2022) 137112. https://doi.org/10.1016/j.cej.2022.137112.

[11] Y. Ma, H. Fan, C. Wu, M. Zhang, J. Yu, L. Song, K. Li, J. He, An efficient dual-metal single-atom catalyst for bifunctional catalysis in zinc-air batteries, Carbon N. Y. 185 (2021) 526–535. https://doi.org/10.1016/j.carbon.2021.09.044.

[12] Y. Wang, B.J. Park, V.K. Paidi, R. Huang, Y. Lee, K.J. Noh, K.S. Lee, J.W. Han, Precisely Constructing Orbital Coupling-Modulated Dual-Atom Fe Pair Sites for Synergistic CO2 Electroreduction, ACS Energy Lett. 7 (2022) 640–649. https://doi.org/10.1021/acsenergylett.1c02446.

[13] L. Yu, F. Li, J. Zhao, Z. Chen, Revisiting catalytic performance of supported metal dimers for oxygen reduction reaction via magnetic coupling from first principles, Adv. Powder Mater. 1 (2022) 100031. https://doi.org/10.1016/j.apmate.2022.01.004.

[14] F. Kong, R. Si, N. Chen, Q. Wang, J. Li, G. Yin, M. Gu, J. Wang, L.M. Liu, X. Sun, Origin of hetero-nuclear Au-Co dual atoms for efficient acidic oxygen reduction, Appl. Catal. B Environ. 301 (2022) 120782. https://doi.org/10.1016/j.apcatb.2021.120782.

[15] Y. Li, B. Wei, M. Zhu, J. Chen, Q. Jiang, B. Yang, Y. Hou, L. Lei, Z. Li, R. Zhang, Y. Lu, Synergistic Effect of Atomically Dispersed Ni–Zn Pair Sites for Enhanced CO2 Electroreduction, Adv. Mater. 33 (2021) 1–12. https://doi.org/10.1002/adma.202102212.

[16] T. He, B. Yu, Y. Zhang, X. Ouyang, S. Chen, Rational design of carbon-supported single and dual atom catalysts for bifunctional oxygen electrocatalysis, Curr. Opin. Electrochem. (2022) 101197.

[17] T. He, A.R.P. Santiago, Y. Kong, M.A. Ahsan, R. Luque, A. Du, H. Pan, Atomically

Dispersed Heteronuclear Dual-Atom Catalysts: A New Rising Star in Atomic Catalysis, Small. 2106091 (2021). https://doi.org/10.1002/smll.202106091.

[18] W. Li, J. Yang, D. Wang, Long-Range Interactions in Diatomic Catalysts Boosting Electrocatalysis, Angew. Chemie. 202213318 (2022). https://doi.org/10.1002/ange.202213318.

[19] G. Yang, J. Zhu, P. Yuan, Y. Hu, G. Qu, B.A. Lu, X. Xue, H. Yin, W. Cheng, J. Cheng, W. Xu, J. Li, J. Hu, S. Mu, J.N. Zhang, Regulating Fe-spin state by atomically dispersed Mn-N in Fe-N-C catalysts with high oxygen reduction activity, Nat. Commun. 12 (2021) 4–13. https://doi.org/10.1038/s41467-021-21919-5.

[20] L. Jiao, J. Zhu, Y. Zhang, W. Yang, S. Zhou, A. Li, C. Xie, X. Zheng, W. Zhou, S.H. Yu, H.L. Jiang, Non-Bonding Interaction of Neighboring Fe and Ni Single-Atom Pairs on MOF-Derived N-Doped Carbon for Enhanced CO2Electroreduction, J. Am. Chem. Soc. 143 (2021) 19417–19424. https://doi.org/10.1021/jacs.1c08050.

[21] J. Zhao, L. Zong, L. Cui, F. Lu, Z. Xiao, L. Wang, Synthesis of Dual-metal Single Atom in Porous Carbon Nanospheres with Enhanced Oxygen Reduction Activity in Both Acidic and Alkaline Electrolytes, J. Colloid Interface Sci. (2022). https://doi.org/10.1016/j.jcis.2022.11.147.

[22] M. Tong, F. Sun, Y. Xie, Y. Wang, Y. Yang, C. Tian, L. Wang, H. Fu, Operando Cooperated Catalytic Mechanism of Atomically Dispersed Cu−N4 and Zn−N4 for Promoting Oxygen Reduction Reaction, Angew. Chemie - Int. Ed. 60 (2021) 14005–14012. https://doi.org/10.1002/anie.202102053.

[23] W.S. Hummers, R.E. Offeman, Preparation of Graphitic Oxide, J. Am. Chem. Soc. 80 (1958) 1339. https://doi.org/10.1021/ja01539a017.

[24] M.D. Hossain, Z. Liu, M. Zhuang, X. Yan, G.L. Xu, C.A. Gadre, A. Tyagi, I.H. Abidi, C.J. Sun, H. Wong, A. Guda, Y. Hao, X. Pan, K. Amine, Z. Luo, Rational Design of Graphene-Supported Single Atom Catalysts for Hydrogen Evolution Reaction, Adv. Energy Mater. 9 (2019). https://doi.org/10.1002/aenm.201803689.

[25] K. Khan, T. Liu, M. Arif, X. Yan, M.D. Hossain, F. Rehman, S. Zhou, J. Yang, C. Sun,

S.H. Bae, J. Kim, K. Amine, X. Pan, Z. Luo, Laser-Irradiated Holey Graphene-Supported Single-Atom Catalyst towards Hydrogen Evolution and Oxygen Reduction, Adv. Energy Mater. 2101619 (2021) 1–9. https://doi.org/10.1002/aenm.202101619.

[26] X. Hai, S. Xi, S. Mitchell, K. Harrath, H. Xu, D.F. Akl, D. Kong, J. Li, Z. Li, T. Sun, H. Yang, Y. Cui, C. Su, X. Zhao, J. Li, J. Pérez-ramírez, J. Lu, Scalable two-step annealing method for preparing ultra-high-density single-atom catalyst libraries, (n.d.). https://doi.org/10.1038/s41565-021-01022-y.

[27] A. V. Marenich, C.J. Cramer, D.G. Truhlar, Universal solvation model based on solute electron density and on a continuum model of the solvent defined by the bulk dielectric constant and atomic surface tensions, J. Phys. Chem. B. 113 (2009) 6378–6396. https://doi.org/10.1021/jp810292n.

[28] T. Lu, F. Chen, Multiwfn: A multifunctional wavefunction analyzer, J. Comput. Chem. 33 (2012) 580–592. https://doi.org/10.1002/jcc.22885.

[29] K. Khan, X. Yan, Q. Yu, S.H. Bae, J.J. White, J. Liu, T. Liu, C. Sun, J. Kim, H.M. Cheng, Y. Wang, B. Liu, K. Amine, X. Pan, Z. Luo, Stone-Wales defect-rich carbon-supported dual-metal single atom sites for Zn-air batteries, Nano Energy. 90 (2021) 106488. https://doi.org/10.1016/j.nanoen.2021.106488.

[30] X. Li, C.S. Cao, S.F. Hung, Y.R. Lu, W. Cai, A.I. Rykov, S. Miao, S. Xi, H. Yang, Z. Hu, J. Wang, J. Zhao, E.E. Alp, W. Xu, T.S. Chan, H. Chen, Q. Xiong, H. Xiao, Y. Huang, J. Li, T. Zhang, B. Liu, Identification of the Electronic and Structural Dynamics of Catalytic Centers in Single-Fe-Atom Material, Chem. 6 (2020) 3440–3454. https://doi.org/10.1016/j.chempr.2020.10.027.

[31] H. Xu, D. Cheng, D. Cao, X.C. Zeng, A universal principle for a rational design of single-atom electrocatalysts, Nat. Catal. 1 (2018) 339–348. https://doi.org/10.1038/s41929-018-0063-z.

[32] A. Kulkarni, S. Siahrostami, A. Patel, J.K. Nørskov, Understanding Catalytic Activity Trends in the Oxygen Reduction Reaction, Chem. Rev. 118 (2018) 2302–2312. https://doi.org/10.1021/acs.chemrev.7b00488.

[33] J. Zhang, A. Yu, C. Sun, Computational Exploration of Dual Atom Catalysts Loaded on Defective Graphene for Oxygen Reduction Reaction, Appl. Surf. Sci. (2022) 154534. https://doi.org/10.1016/j.apsusc.2022.154534.

[34] G. Di Liberto, S. Tosoni, L.A. Cipriano, G. Pacchioni, A Few Questions about Single-Atom Catalysts : When Modeling Helps, (2022). https://doi.org/10.1021/accountsmr.2c00118.

[35] Y. Ying, K. Fan, X. Luo, J. Qiao, H. Huang, Unravelling the origin of bifunctional OER/ORR activity for single-atom catalysts supported on C 2 N by DFT and machine learning , J. Mater. Chem. A. (2021) 16860–16867. https://doi.org/10.1039/d1ta04256d.

[36] Y. Zhang, Y. Cheng, X. Wang, Q. Sun, X. He, H. Ji, Enhanced Hydrogenation Properties of Pd Single Atom Catalysts with Atomically Dispersed Ba Sites as Electronic Promoters, ACS Catal. (2022) 15091–15096. https://doi.org/10.1021/acscatal.2c04626.

[37] S. Chen, T. Luo, X. Li, K. Chen, J. Fu, K. Liu, C. Cai, Q. Wang, H. Li, Y. Chen, C. Ma, L. Zhu, Y. Lu, T. Chan, M. Zhu, E. Cort, M. Liu, Identification of the Highly Active Co − N 4 Coordination Motif for Selective Oxygen Reduction to Hydrogen Peroxide, (2022). https://doi.org/10.1021/jacs.2c01194.

[38] M. Zhang, H. Li, J. Chen, F. Ma, L. Zhen, Z. Wen, C. Xu, Transition Metal (Co , Ni , Fe , Cu) Single-Atom Catalysts Anchored on 3D Nitrogen-Doped Porous Carbon Nanosheets as Efficient Oxygen Reduction Electrocatalysts for Zn – Air Battery, 2202476 (2022) 1–10. https://doi.org/10.1002/smll.202202476.

[39] C. Zhang, Y. Dai, Q. Sun, C. Ye, R. Lu, Y. Zhou, Y. Zhao, Strategy to weaken the oxygen adsorption on single-atom catalysts towards oxygen-involved reactions, Mater. Today Adv. 16 (2022) 100280. https://doi.org/10.1016/j.mtadv.2022.100280.

[40] H. Bin Yang, S.F. Hung, S. Liu, K. Yuan, S. Miao, L. Zhang, X. Huang, H.Y. Wang, W. Cai, R. Chen, J. Gao, X. Yang, W. Chen, Y. Huang, H.M. Chen, C.M. Li, T. Zhang, B. Liu, Atomically dispersed Ni(i) as the active site for electrochemical CO2 reduction, Nat. Energy. 3 (2018) 140–147. https://doi.org/10.1038/s41560-017-0078-8.

[41] X. Wang, Y. Fu, D. Tranca, K. Jiang, J. Zhu, J. Zhang, S. Han, C. Ke, C. Lu, X. Zhuang,

Regulating the Spin State of Nickel in Molecular Catalysts for Boosting Carbon Dioxide Reduction, ACS Appl. Energy Mater. 4 (2021) 2891–2898. https://doi.org/10.1021/acsaem.1c00269.

[42] Y.N. Gong, W. Zhong, Y. Li, Y. Qiu, L. Zheng, J. Jiang, H.L. Jiang, Regulating photocatalysis by spin-state manipulation of cobalt in covalent organic frameworks, J. Am. Chem. Soc. 142 (2020) 16723–16731. https://doi.org/10.1021/jacs.0c07206.

[43] W. Wan, Y. Zhao, S. Wei, C.A. Triana, J. Li, A. Arcifa, C.S. Allen, R. Cao, G.R. Patzke, Mechanistic insight into the active centers of single/dual-atom Ni/Fe-based oxygen electrocatalysts, Nat. Commun. 12 (2021) 1–13. https://doi.org/10.1038/s41467-021-25811-0.

[44] B. Wang, J. Tang, X. Zhang, M. Hong, H. Yang, X. Guo, S. Xue, C. Du, Z. Liu, J. Chen, Nitrogen doped porous carbon polyhedral supported Fe and Ni dual-metal single-atomic catalysts: template-free and metal ligand-free sysnthesis with microwave-assistance and d-band center modulating for boosted ORR catalysis in zinc-air batteries, Chem. Eng. J. 437 (2022) 135295. https://doi.org/10.1016/j.cej.2022.135295.

[45] L. Jiao, J. Zhu, Y. Zhang, W. Yang, S. Zhou, A. Li, C. Xie, X. Zheng, W. Zhou, S. Yu, H. Jiang, Non-Bonding Interaction of Neighboring Fe and Ni Single-Atom Pairs on MOF-Derived N - Doped Carbon for Enhanced CO 2 Electroreduction, (2021). https://doi.org/10.1021/jacs.1c08050.

[46] O. Bunău, Y. Joly, Self-consistent aspects of x-ray absorption calculations, J. Phys. Condens. Matter. 21 (2009). https://doi.org/10.1088/0953-8984/21/34/345501.

[47] M.D. Hossain, Z. Liu, M. Zhuang, X. Yan, G.L. Xu, C.A. Gadre, A. Tyagi, I.H. Abidi, C.J. Sun, H. Wong, A. Guda, Y. Hao, X. Pan, K. Amine, Z. Luo, Rational Design of Graphene-Supported Single Atom Catalysts for Hydrogen Evolution Reaction, Adv. Energy Mater. 9 (2019) 1–10. https://doi.org/10.1002/aenm.201803689.

[48] A. Eckmann, A. Felten, I. Verzhbitskiy, R. Davey, C. Casiraghi, Raman study on defective graphene: Effect of the excitation energy, type, and amount of defects, Phys. Rev. B - Condens. Matter Mater. Phys. 88 (2013) 1–11.

https://doi.org/10.1103/PhysRevB.88.035426.

[49] Z. Zhu, H. Yin, Y. Wang, C.H. Chuang, L. Xing, M. Dong, Y.R. Lu, G. Casillas-Garcia, Y. Zheng, S. Chen, Y. Dou, P. Liu, Q. Cheng, H. Zhao, Coexisting Single-Atomic Fe and Ni Sites on Hierarchically Ordered Porous Carbon as a Highly Efficient ORR Electrocatalyst, Adv. Mater. 32 (2020) 1–8. https://doi.org/10.1002/adma.202004670.

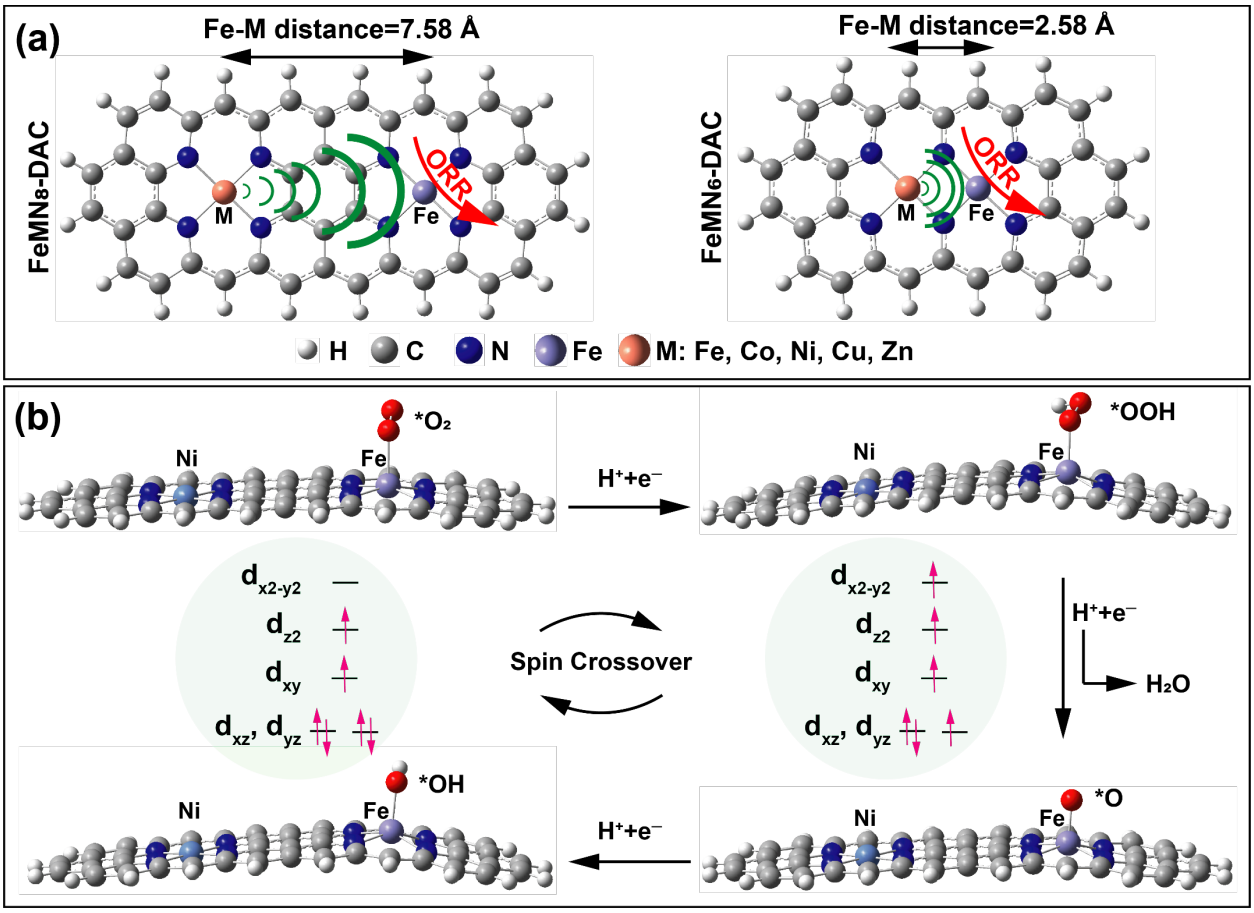

Scheme1. Schematic for the application of DACs to ORR. (a) The structure of $FeMN_6$-DAC and $FeMN_8$-DAC (Gray colors balls: carbon, dark blue: nitrogen, red: oxygen, cream: hydrogen, blue: iron, and salmon: counterpart M metal (Fe, Co, Ni, Cu, and Zn)). (b) Lateral view of reaction intermediates along the ORR pathway for $FeNiN_8$-DAC, indicating the spin crossover during the reaction. This further indicates the effect of non-bonding effect of counterpart metals on the catalytic activity of Fe active site.

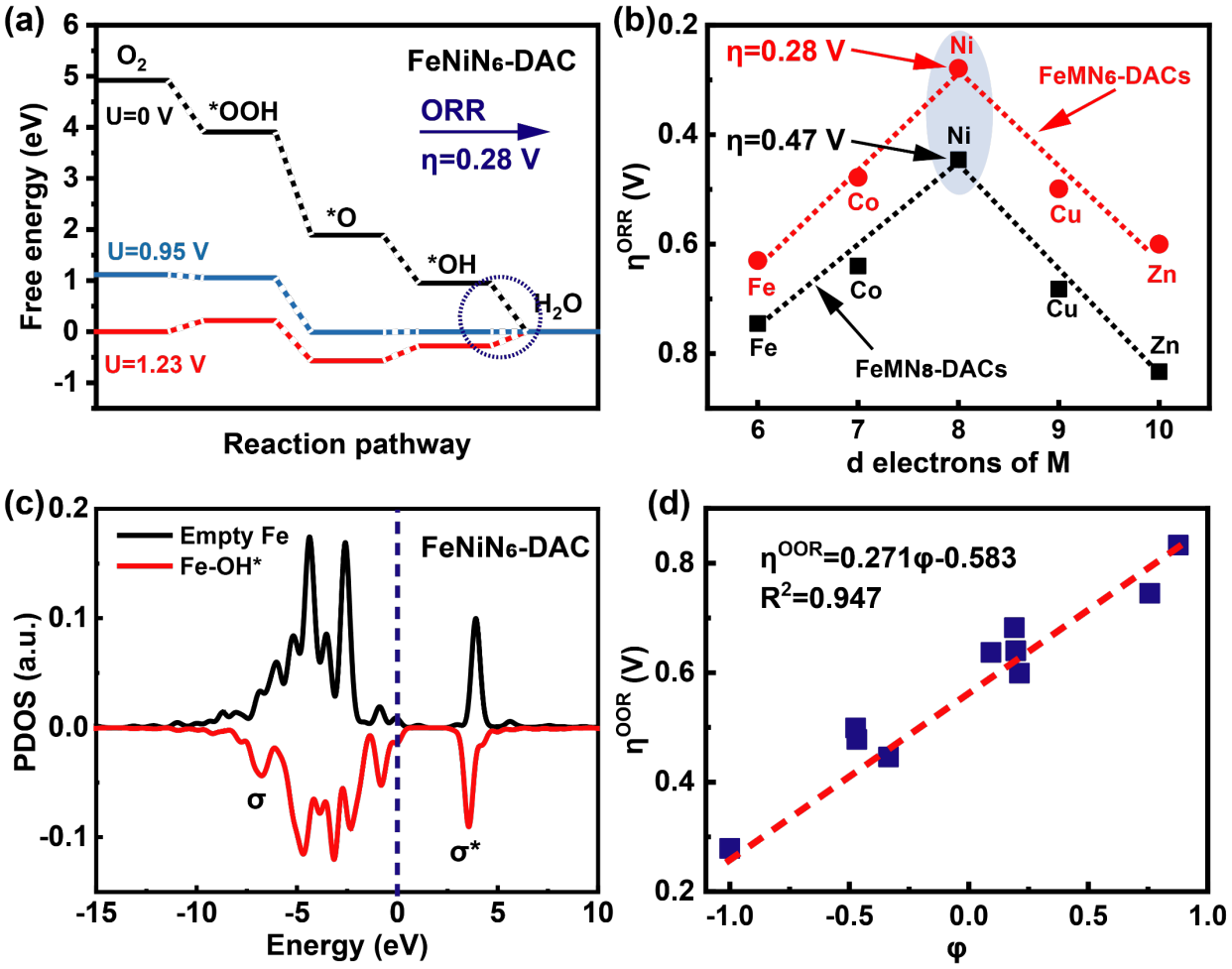

Figure 1. DFT calculations results. (a) The Gibbs free energy diagram for oxygen reduction reaction (ORR) corresponding to $FeNiN_6$-DAC with the ORR overpotentials (η^{ORR}) of 0.28 V, shown in blue circle. (b) Volcano plot of theoretical ORR overpotential (η^{ORR}) versus the d electrons of counterpart metal for $FeMN_6$-DAC and $FeMN_8$-DAC structures, indicating $FeNiN_6$-DAC and $FeNiN_8$-DAC at the summits. (c) PDOS of 3d hybrid orbital of Fe atom in $FeNiN_6$-DAC before and after interaction with OH*, indicating the bonding (σ) and antibonding (σ*) orbitals after interaction with OH*. (d) Overpotential (η^{ORR}) of $FeMN_6$-DAC and $FeMN_8$-DAC versus the new descriptor (φ), suggesting the new descriptor satisfactory defines the linear relationship with the η^{ORR} for DACs.

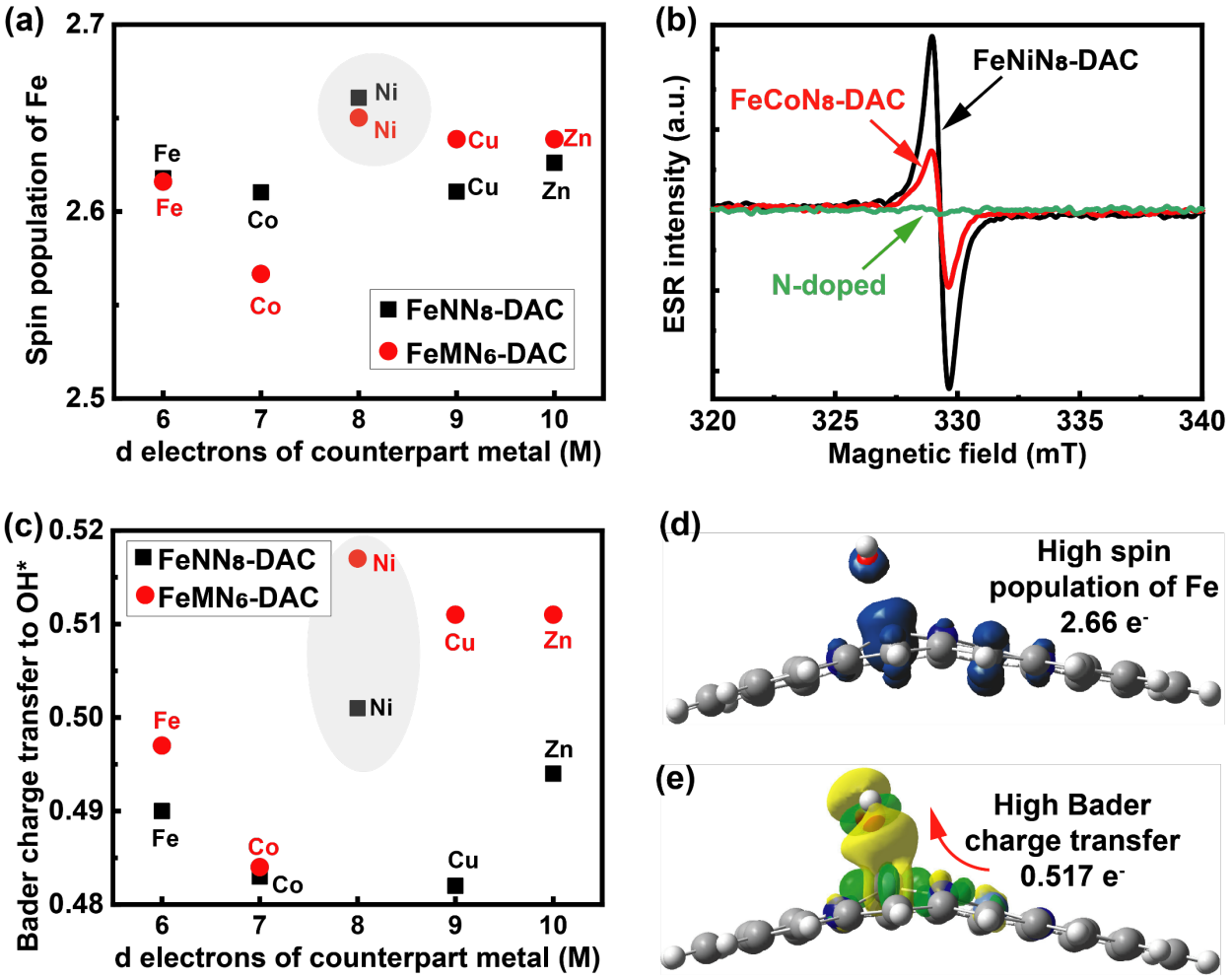

Figure 2. Spin population and Bader charge transfer analysis. (a) The spin population of Fe atom (Fe-OH*) versus d electrons of counterpart metals (M), indicating $FeNiN_6$-DAC and $FeNiN_8$-DAC at the top with higher spin density. (b) Electron spin resonance (ESR) spectra of samples measured at 77 K, indicating higher spin population for $FeNiN_8$-DAC compared to $FeCoN_8$-DAC and no peak for N-doped sample. (c) Bader charge transfer from Fe site to OH* intermediate versus the d electrons of counterpart metal (M). (d) The spatial spin density of $FeNiN_6$-DAC (Isosurface value = 0.015 e/Å^3). Blue and green colors represent the alpha and beta spin density, respectively. (e) Side view of charge transfer within the system of $FeNiN_6$-DAC (Isosurface value = 0.004 e/Å^3). Yellow and green colors represent the charge availability and deficiency, respectively. This indicates the high spin population and high charge transfer ability of $FeNiN_6$-DAC system.

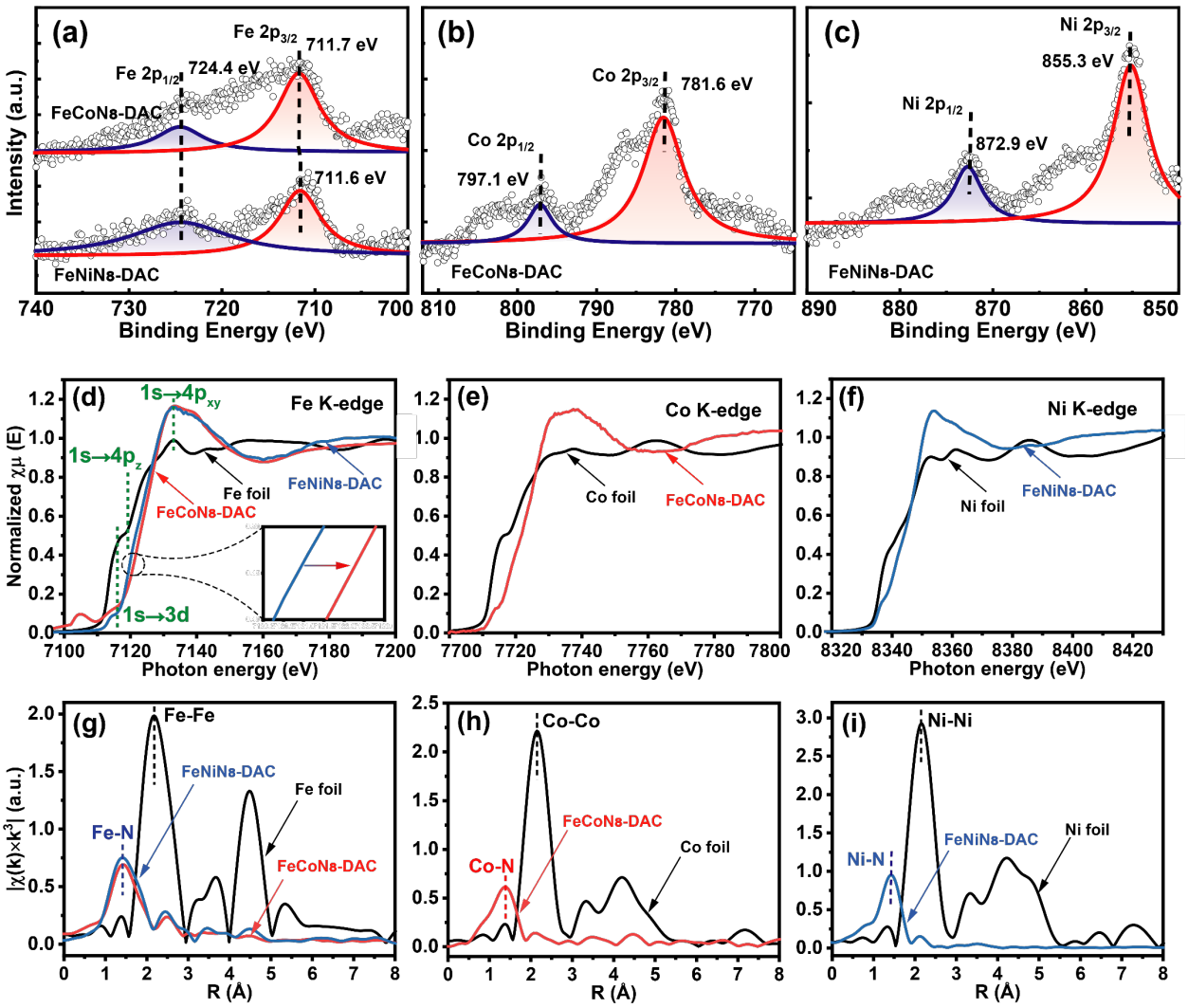

Figure 3. XPS, XANES, and EXAFS characterizations. (a) The Fe 2p, (b) Co 2p, and (c) Ni 2p XPS spectra of synthesized samples, showing two peaks belonging to $2p_{3/2}$ and $2p_{1/2}$. The binding energy of Fe, Co, and Ni indicates their oxidation state of higher than 0. (d) Fe K-edge, (e) Co K-edge, and (f) Ni K-edge XANES spectra of our synthesized samples and their reference bulk samples. Three peaks are corresponded to 1s→3d, 1s→$4p_z$, and 1s→$4p_{xy}$ transitions.[40] Fourier transformations (FT) EXAFS spectra in R space of (g) of Fe, (h) Co, and (i) Ni with their reference bulk samples. The primary peaks attributed to Fe-, Co-, and Ni-N are different from Fe-Fe, Co-Co, and Ni-Ni peaks, respectively.

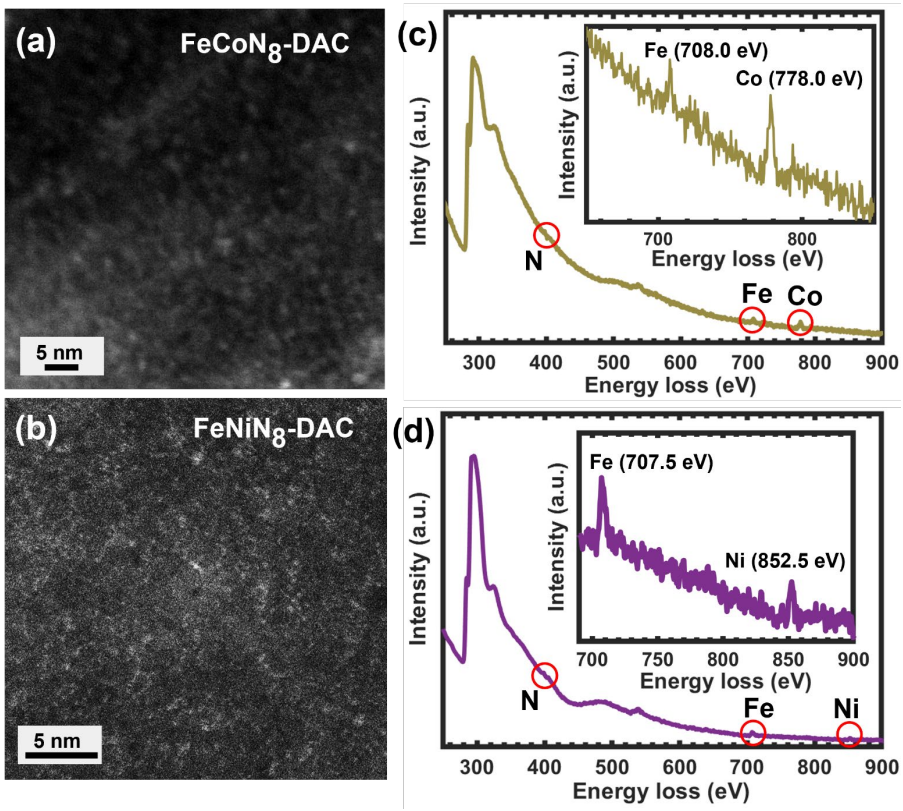

Figure 4. STEM images and EELS characterization. STEM image (a) and EELS analysis (c) of the $FeCoN_8$-DAC sample showing that the individual Fe and Co metal atoms are homogeneously dispersed on the graphene support. STEM image (b) and EELS analysis (d) of the $FeNiN_8$-DAC sample showing that the Fe and Ni metal atoms are homogeneously dispersed on the graphene support.

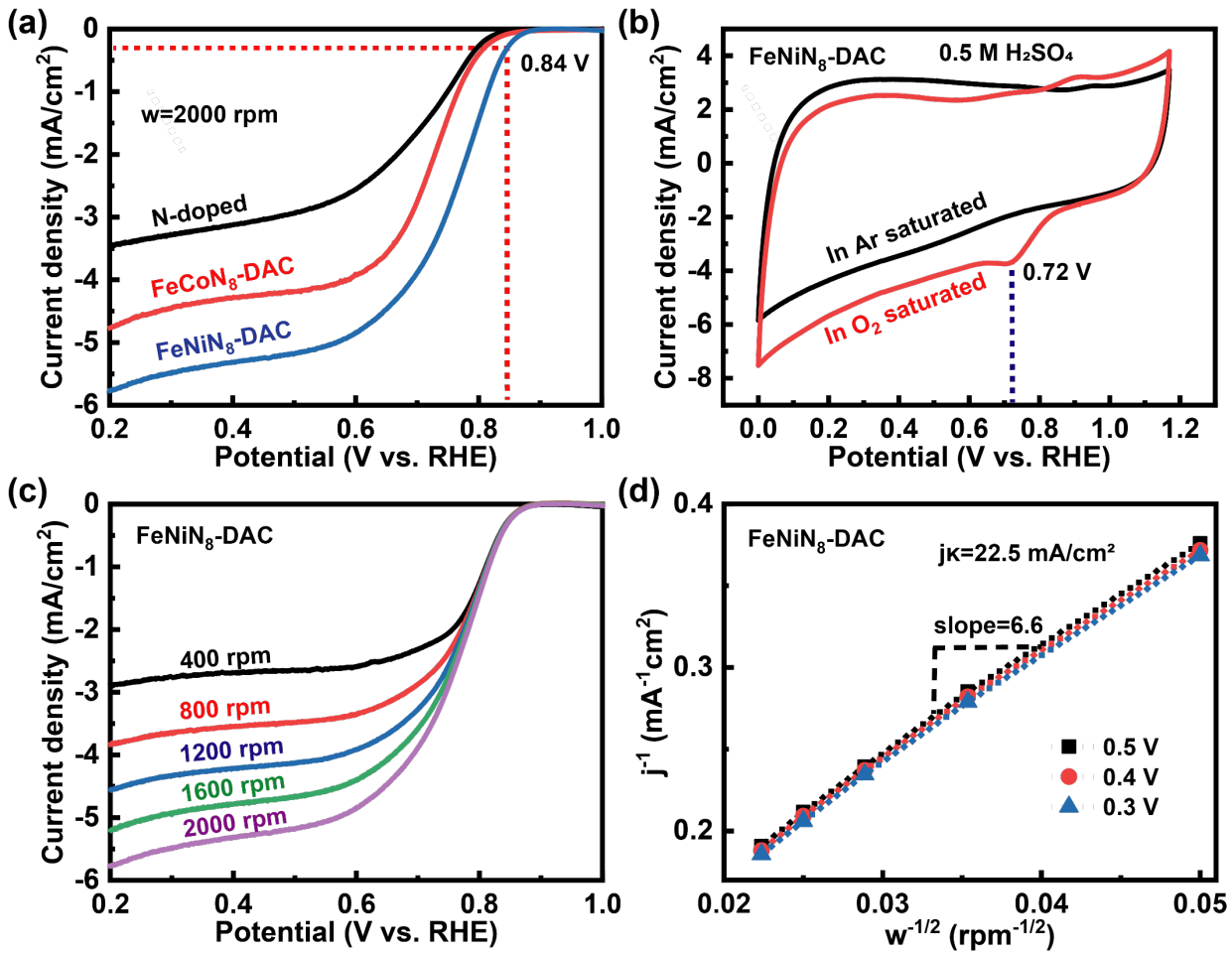

Figure 5. ORR catalytic performance. (a) ORR polarization curves. (b) CV curves for $FeNiN_8$-DAC sample in O_2- and Ar-saturated environment, revealed a prominent ORR peak (red line) at 0.72 V versus RHE. This indicates that O_2 is reduced with the $FeNiN_8$-DAC catalyst. (c) The rotation disk data of the $FeNiN_8$-DAC sample for various rotation speeds. (d) K-L plot for different applied potentials, indicating good linearity with the kinetic current density (j_K) of 22.5 $mAcm^{-2}$. All catalytic performance is measured in an O_2-saturated environment using 0.5 M H_2SO_4.

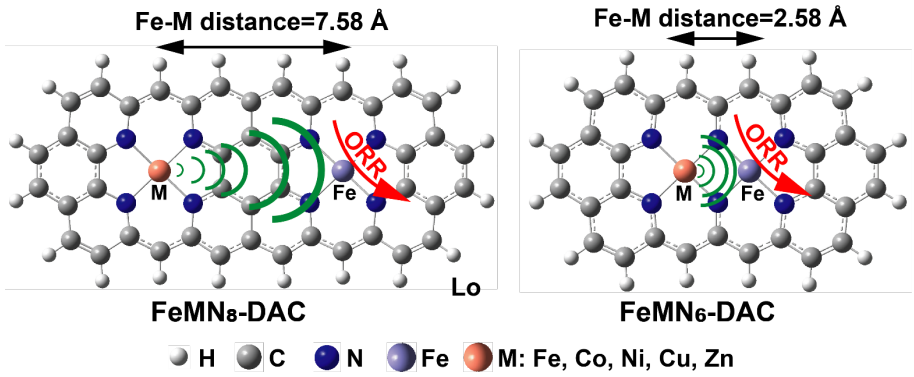

Table of Contents (TOC)